ENCLOSURE-I *Conf-9207115--3* 1

PHASE DISTRIBUTION IN COMPLEX GEOMETRY CONDUITS

R.T. Lahey, Jr.
M. Lopez de Bertodano
O.C. Jones, Jr.
Center for Multiphase Research
Rensselaer Polytechnic Institute
Troy, New York   12180-3590

RECEIVED
JAN 2 7 1994
OSTI

CMR
CMR
CMR
CMR

INTRODUCTION

Some of the most important and challenging problems in two-phase flow today have to do with the understanding and prediction of multidimensional phenomena, in particular, lateral phase distribution in both simple and complex geometry conduits. A prior review paper [1] summarized the state-of-the-art in the understanding of phase distribution phenomena, and the ability to perform mechanistic multidimensional predictions. The purpose of this paper is to update that review, with particular emphasis on complex geometry conduit predictive capabilities.

Previous experimental studies have shown that pronounced lateral phase distribution may occur. Serizawa et al [2] and Michiyoshi et al [3] have measured pronounced wall peaking of the local void fraction for turbulent bubbly air/water two-phase upflow in a pipe. Similar results were found by Valukina et al [4] for laminar bubbly air/water two-phase upflow in a pipe. These results were later confirmed in a study by Wang et al [5], and were extended to show that, in contrast to the bubbly upflow results, void coring (ie, void concentration near the pipe's centerline) occurred for turbulent bubbly two-phase air/water downflow in a pipe.

Recently, the development of these lateral phase distribution profiles has been studied by Class et al [6] and Liu [7], where it was found that bubble size effects are important. This may explain why wall peaking in vertical cocurrent upflow is not always observed.

The importance of bubble size on lateral void phase distribution has also been recognized by other investigators, including Sekoguchi et al [8] and Zun [9]. Moreover, Monji et al [10] have found that for bubbly air/water upflows that small bubbles (D_b < 0.5 mm) tend to be uniformly distributed across the conduits, while large bubbles (D_b > 6 mm) tend to core, and it is only the intermediate size bubbles that concentrate near the wall of the conduit.

Interestingly, similar lateral phase distribution phenomena have also been observed in complex geometry conduits. Sadatomi et al [11] have found pronounced wall peaking for turbulent bubbly air/water two-phase upflow in vertical triangular and rectangular conduits. Moreover, they found that for slug flow, void coring occurred. Similar void coring has been observed by Sim et al [12] for bubbly/slug air/water upflows in a vertical triangular duct.

Okhawa et al [13] made measurements of bubbly air/water two-phase upflow in an eccentric annular test section. They observed significant lateral phase distribution, with the void fraction being larger in the more open region of the flow area. Similar results were found by Shiralkar et al [14] using boiling Freon-114.

It is clear that there are strong lateral forces on the dispersed (ie, vapor) phase which lead to the observed phase distributions. Thus let us next consider what is known about the physics of these lateral forces.

Drew & Lahey have demonstrated the unique relationship between the turbulence field of the liquid phase and the void distribution for pipes [15] and for complex geometry conduits [16]. Similar results have also been found by Kataoka et al [17]. Wang et al [5] have extended these analyses to include other lateral forces such as the so-called lift term, the analytical form of which has been derived by Drew & Lahey [18], [19].

Several distinctly different analytical approaches have been pursued for the prediction of lateral void distribution. A Lagrangian simulation has been proposed by Zun et al [20], and this approach shows promise. Another approach, which is in accordance with what has been widely adopted for nuclear reactor safety analysis,

MASTER

DISCLAIMER

is based on the computational fluid dynamic (CFD) numerical evaluation of a properly formulated multidimensional two-fluid model. This is the approach which will be stressed in this paper.

In a pioneering study Lee et al [21] demonstrated that closed-loop predictions of lateral phase distribution for bubbly upflow in a pipe can be made using a multidimensional two-fluid model and a k-ε turbulence model. Unfortunately, in this study the degree of turbulence non-isotropy and several important boundary conditions had to be specified in order to close the system of equations.

In a subsequent study, Lopez de Bertodano et al [22] performed a mechanistic CFD prediction of lateral phase distribution in pipes using a multidimensional two-fluid model and a Reynolds stress (ie, τ-ε) turbulence model. As noted in a previous review paper [1], this study represents a significant breakthrough since it shows that detailed closed-loop mechanistic predictions of complicated two-phase flow is possible if we have a properly formulated two-fluid model.

Recent research has been completed by Lopez de Bertodano [23] in which lateral phase distribution in complex geometry conduits was studied. In particular, experiments and CFD analysis were performed for a vertical isosceles triangular test section. Let us first consider the data taken in this study.

DISCUSSION - EXPERIMENTAL STUDY

The air/water test loop in which the data were taken is shown schematically in Fig. 1. The test section was an isosceles triangle having 50 mm base and 100 mm height. The duct was 2840 mm long (ie, L/D = 73). The mixing tee, shown schematically in Fig. 2, was used in all tests. This device allowed the control of bubble size. In particular, 5 mm diameter bubbles existed for all sets of data. These air/water data were found to agree with the previous void fraction data of Sadatomi et al [11], and extended this prior study since the turbulent structure of the continuous phase was also measured.

Liquid phase velocity, turbulence and void fraction measurements were made using various TSI hot-film probes. Both a single sensor boundary layer probe and an X-wire Reynolds stress probe were used. The single sensor cylindrical boundary layer probe had a TSI 10 AW element (0.025 mm × 0.25 mm) and the X-wire probe had TSI 10 W elements (0.025 mm × 0.50 mm) which were 0.34 mm apart. The boundary layer probe could be positioned to within 0.10 mm from the conduit wall, which was closer than for the X-wire probe.

The data acquisition system consisted of three TSI 1050 anemometer modules that kept the hot films at a constant temperature. The analog outputs were digitized with a custom-made CAMAC A/D converter board, having three 13-bit A/D converters, that was connected to a VAX-750 computer. The A/D converters were triggered simultaneously by a Kinetic Systems CAMAC 3655 Timing Pulse Generator. Kolmogorov [24] scaling indicated that a 10 kHz sampling rate was sufficient to capture all significant scales of turbulence, and this sampling rate was used for all data.

A schematic of the probe's traversing mechanism is shown in Fig. 3. It consisted of a rotating drum housing and a rotating ball on the side that the probe penetrated through. The probe was moved in and out using a micrometer having 0.025 mm. graduations. The probe had a 90° bend and an extension piece so that the sensors were located within the test section approximately 3 L/D from the exit. This arrangement gave three degrees of freedom so that the probe could be located at any position and orientation in the cross section. The ability to freely orient the probe was important since one must set the boundary layer probe with its measurement wire parallel to the wall, and position the X-wire probe in the appropriate direction to measure the various Reynolds stresses.

CALIBRATION

The single sensor one mil diameter boundary layer probe was calibrated for void fraction using a gamma-ray densitometer having a 10 Ci Cs-137 source and a NaI scintillating detector connected to a multichannel analyzer. Probe calibration was done following the technique of Sim & Lahey [25], and the results of this calibration are shown in Fig. 4 together with previous results by Lee et al [27].

After performing a careful error analysis it was determined that the error in the gamma ray measurement of void fraction was negligible compared to the error in the hot film measurement so the error bars shown in Fig. 4 correspond to the hot film data. Since the gamma-ray measurement was taken across the test-section's width many hot film measurements had to be taken and averaged along the gamma-ray path when comparisons were made. In addition, by taking two measurements at each point it was possible to obtain the standard derivation of the chordal-averaged void fraction. We note that the deviation (ε) for the boundary layer probe is fairly low and remains approximately constant around a value of ± 6% of point.

The velocity calibration of the hot film probes was performed using a calibration nozzle assembly. A 6.35 mm (1/4 in.) diameter nozzle was used. The pressure drop across the nozzle was measured using a Validyne pressure transducer. The velocity at the nozzle exit was calculated directly using the Bernoulli equation. This is valid everywhere except in the thin boundary layer around the nozzle wall. The water temperature in the nozzle assembly was measured using a mercury thermometer having 0.1°C temperature graduations. Because of probe signal drift it was also necessary to perform periodic on-line recalibrations with a pitot tube.

TEST PROCEDURE

Hot film anemometry has proven very valuable in liquid/vapor flows since the hot film simultaneously measures the phase indicator function and the instantaneous liquid velocity. The signals can be time-averaged to obtain the local void fraction, average velocity and turbulence quantities. Figure 5 shows a typical signal, the corresponding vapor phase indicator function and the velocity of the liquid phase. Following the work of Lee et al [26] and Wang [27] the penetration of a bubble by the probe was determined using both a signal level and a slope thresholding criteria. When a bubble approaches the probe, surface tension causes it to deform. Thus, as can be seen in Fig. 5, immediate penetration of the interface does not occur. The gamma-ray densitometer calibration experiments discussed previously were carried out to account for this effect. The liquid velocity was computed from the probe output voltage using King's Law:

$$Nu = A + BRe^n$$

where the correlation parameters A, B and n were obtained from the calibration nozzle measurements.

The X-wire probe was used to measure the instantaneous velocity components lying in the plane of the wires. If the X-probe lies in the x-y plane then the mean liquid velocity components, $\bar{u}$ and $\bar{v}$, and the Reynolds stress components, $\overline{u'u'}$, $\overline{v'v'}$ and $\overline{u'v'}$, are measured. By rotating the probe 90° about the vertical axis the remaining velocity component $\bar{w}$ and the Reynolds stress components $\overline{w'w'}$ and $\overline{u'w'}$ are obtained. Only the shear stress in the horizontal plane, $\overline{v'w'} = \overline{w'v'}$, was not measured, however in duct flows this shear stress is about two orders of magnitude smaller than the other components and was thus negligible.

The effective velocity (u_{eff}) measured by a sensor "i" is:

$$u_{eff}^2 = u_i^2 + k_y^2 v_i^2 + k_z^2 w_i^2 \tag{1}$$

where k_x and k_y are geometric cooling factors and, as can be seen in Fig. 6, u_i, v_i and w_i are the velocity components with respect to the sensor's coordinate system (x',y',z'). To convert from the sensor's coordinate system to a reference coordinate system (x,y,z) the following transformation was used:

$$\begin{pmatrix} u_i \\ v_i \\ w_i \end{pmatrix} = \begin{pmatrix} -\cos\theta_i \sin\psi_i & -\sin\theta_i \sin\psi_i & \cos\psi_i \\ \cos\theta_i \cos\psi_i & \sin\theta_i \cos\psi_i & \sin\psi_i \\ -\sin\theta_i & \cos\theta_i & 0 \end{pmatrix} \begin{pmatrix} u \\ v \\ w \end{pmatrix} \tag{2}$$

For the case of the X-wire probe, setting $\theta_1 = \theta_2 = 0$ and $-\psi_1 = \psi_2 = \pi/4$ yields:

$$\begin{pmatrix} u_1 \\ v_1 \\ w_1 \end{pmatrix} = \sqrt{1/2} \begin{pmatrix} u + w \\ u - w \\ \sqrt{2}\, v \end{pmatrix} \qquad , \qquad \begin{pmatrix} u_2 \\ v_2 \\ w_2 \end{pmatrix} = \sqrt{1/2} \begin{pmatrix} -u + w \\ u + w \\ \sqrt{2}\, v \end{pmatrix} \tag{3}$$

Combining these equations yields, after some algebra:

$$(1 + k_y^2)(u^2 + w^2) + 2k_z^2 v^2 = u_{eff_1}^2 + u_{eff_2}^2 \tag{4a}$$

$$2(1 - k_y^2)\, uw = u_{eff_1}^2 - u_{eff_2}^2 \tag{4b}$$

For duct flow $u \gg v$ & w so these equations imply:

$$u \cong \sqrt{\frac{u_{eff_1}^2 + u_{eff_2}^2}{1 + k_y^2}} \tag{5}$$

and,

$$w \cong \frac{\left(u_{eff_1}^2 - u_{eff_2}^2 \right)}{2(1 - k_y^2)} \sqrt{\frac{1 + k_y^2}{u_{eff_1}^2 + u_{eff_2}^2}} \tag{6}$$

Thus the instantaneous values of u and w can be obtained from the measured u_{eff_i}, hence $\bar{u}$, $\bar{w}$, $\overline{u'u'}$, $\overline{w'w'}$ and $\overline{u'w'}$ can be computed.

The so-called yaw factor, k_y, has been measured by Jorgensen [28] for a variety of wire geometries. For a DISA 55F26 sensor at any angle of 45° to the flow, $k_y = 0.4$. This sensor had the same aspect ratio as the sensors used in the X-wire probe and thus this value of k_y was used in all data reduction.

THE DATA

The single wire boundary layer probe was used to measure the local void fraction and the axial liquid velocity. The X-sensor probe was used to also measure the local void fraction and axial liquid velocity, and the lateral velocities and the Reynolds stresses were measured.

Flow symmetry tests were performed with the single sensor probe. Some typical measurements (for two different distances from the base of the isosceles triangle) are shown in Figs.-7 and 8. It can be seen that the two-phase flow was symmetric.

Figures 9-13 are graphical representations of typical data. Notice that for the $j_g = 0.05$ m/s case the void fraction peaks near the conduit walls and in the corners, as was previously observed by Sadatomi et al [11]. Also the two-phase velocity profile is flatter than for single-phase flows because of the void peaks near the walls. Interestingly, at $j_g = 0.4$ m/s the void peaks are less pronounced than for $j_g = 0.05$ m/s, and consequently the velocity profile becomes less flat.

A comparison of the single-phase velocity measurements of the boundary layer probe and the X-sensor probe along the apex bisector is given in Fig.-14. Good agreement can be noted, which supports probe calibration and data reduction procedures.

Figures 15-18 are graphical representations of the Reynolds stresses measured. It can be noted that the shear stress, $-\rho_\ell \overline{u'v'}$, in Fig. 17 is in general agreement with the corresponding velocity distribution in Fig. 10. That is, it is approximately zero in the region where the velocity profile is flat, is positive near the base of the triangle where the velocity gradient is positive and negative near the vertex.

DISCUSSION - ANALYSIS

Let us next consider a general three-dimensional two-fluid model for air/water bubbly flows. In this paper an ensemble [29] and cell-averaging [30] approach was used to obtain the phasic continuity and momentum equation as [31]:

$$\frac{\partial(\alpha_g \rho_g)}{\partial t} + \nabla \cdot (\alpha_g \rho_g \underline{v}_g) = 0 \tag{7a}$$

$$\frac{\partial(\alpha_\ell \rho_\ell)}{\partial t} + \nabla \cdot (\alpha_\ell \rho_\ell \underline{v}_\ell) = 0 \tag{7b}$$

$$\frac{\partial}{\partial t}(\alpha_g \rho_g \underline{v}_g) + \nabla \cdot (\alpha_g \rho_g \underline{v}_g \underline{v}_g) = \nabla \cdot [\alpha_g \underline{\sigma}_s]$$

$$- \alpha_g \nabla p_\ell - C_{vm} \alpha_g \rho_\ell \, \underline{a}_{vm} - C_{rot} \alpha_g \rho_\ell \underline{v}_r \times \nabla \times \underline{v}_g$$

$$- C_{vm}^* \rho_\ell \underline{v}_r \left(\frac{D_g \alpha_g}{Dt} + \alpha_g \nabla \cdot \underline{v}_r \right) - (C_1 - 2C_p) \alpha_g \rho_\ell \underline{v}_r \cdot \nabla \underline{v}_r^T$$

$$- C_2 \alpha_g \rho_\ell \underline{v}_r \cdot \left[\nabla \underline{v}_r + \nabla \underline{v}_r^T + (\nabla \cdot \underline{v}_r) \underline{\underline{I}} \right] - b_s \rho_\ell (\underline{v}_r \cdot \underline{v}_r) \nabla \alpha_g$$

$$- a_s \rho_\ell (\underline{v}_r \cdot \nabla \alpha_g) \underline{v}_r - C_L \rho_\ell \alpha_g \underline{v}_r \times \nabla \times \underline{v}_\ell + \alpha_g \rho_g \underline{g} - \frac{3}{8} \frac{C_D}{R_b} \rho_\ell \alpha_g \underline{v}_r |\underline{v}_r|$$

$$- \underline{M}_{gi}^{TD} - \underline{M}_{gw}^{D} - \underline{M}_{gw}^{W} + \underline{M}_{gw}^{W} \tag{8a}$$

$$\frac{\partial}{\partial t}(\alpha_\ell \rho_\ell \underline{v}_\ell) + \nabla \cdot (\alpha_\ell \rho_\ell \underline{v}_\ell \underline{v}_\ell) = \nabla \cdot \left[\alpha_\ell \left(\underline{\underline{\tau}}_{\ell(BI)}^{Re} + \underline{\underline{\tau}}_{\ell(SI)}^{Re} \right) \right]$$

$$- \alpha_\ell \nabla p_\ell - C_p \rho_\ell |\underline{v}_r|^2 \nabla \alpha_\ell + C_{vm} \alpha_g \rho_\ell \underline{a}_{vm} + C_{rot} \alpha_g \rho_\ell (\underline{v}_r \times \nabla \times \underline{v}_g)$$

$$+ C_{vm}^* \rho_\ell \underline{v}_r \left(\frac{D_g \alpha_g}{Dt} + \alpha_g \nabla \cdot \underline{v}_r \right) + C_1 \alpha_g \rho_\ell \underline{v}_r \cdot \nabla \underline{v}_r^T$$

$$+ C_2 \alpha_g \rho_\ell \underline{v}_r \cdot \left[\nabla \underline{v}_r + \nabla \underline{v}_r^T + (\nabla \cdot \underline{v}_r) \underline{\underline{I}} \right]$$

$$+ b_s \rho_\ell (\underline{v}_r \cdot \underline{v}_r) \nabla \alpha_g + a_s \rho_\ell (\underline{v}_r \cdot \nabla \alpha_g) \underline{v}_r + C_L \rho_\ell \alpha_g \underline{v}_r \times \nabla \times \underline{v}_\ell$$

$$+ \alpha_\ell \rho_\ell \, \underline{g} + \frac{3}{8} \frac{C_D}{R_b} \, \rho_\ell \, \alpha_g \, \underline{v}_r \, |\underline{v}_r| - M_{\ell i}^{TD} - M_{\ell w}^{D} - M_{\ell w} + M_{\ell w}^{W} \tag{8b}$$

Let us now consider the closure laws and parameters used in these phasic momentum equations. In particular, those for adiabatic (ie, air/water) bubbly two-phase flow. The total Reynolds stress for the continuous liquid phase is given by,

$$\underline{\tau}_\ell^{Re} = \underline{\tau}_{\ell(BI)}^{Re} + \underline{\tau}_{\ell(SI)}^{Re} \tag{9}$$

where, the bubble-induced shear stress is [32],

$$\underline{\tau}_{\ell(BI)}^{Re} = \rho_\ell \alpha_g \left[a_\ell \, \underline{v}_r \underline{v}_r + b_\ell (\underline{v}_r \cdot \underline{v}_r) \, \underline{I} \right] \tag{10}$$

and, for noninteracting spherical bubbles, the bubble-induced turbulence parameters are [33],

$$a_\ell = -\frac{1}{20} \quad , \text{ and, } \quad b_\ell = -\frac{3}{20}$$

The shear-induced Reynolds stress, $\underline{\tau}_{\ell(SI)}^{Re}$, may come from a k-$\varepsilon$ model and an algebraic stress law [34], or a Reynolds stress (ie, τ-ε) model [22].

An adequate turbulence model for bubbly flow appears to be [23],

$$\alpha_\ell \frac{D_\ell k_{\ell(SI)}}{Dt} = \alpha_\ell (\nabla \cdot \underline{D} + P - \varepsilon) \tag{11}$$

$$\alpha_\ell \frac{D_\ell k_{\ell(BI)}}{Dt} = \alpha_\ell \nabla \cdot \upsilon_t \nabla k_b + \frac{1}{\tau_b} (k_{\ell(BI)_a} - k_{\ell(BI)}) \tag{12}$$

(a first order relaxation model)

$$\alpha_\ell \frac{D_\ell \varepsilon}{Dt} = \alpha_\ell (\nabla \cdot \underline{D}_\varepsilon + P_\varepsilon - \varepsilon_\varepsilon) \tag{13}$$

where, $\underline{D}$, P, $\underline{D}_\varepsilon$, P_ε and ε_ε are parameters defined in classical single-phase k-ε models [34], and,

$$\tau_b = \overline{D}_b / |\underline{v}_r| \tag{14}$$

$$k_{\ell(BI)_a} = \alpha_g \alpha_\ell \, C_p \, |\underline{v}_r|^2 \tag{15}$$

$$k_\ell = k_{\ell(SI)} + k_{\ell(BI)} \tag{16}$$

$$\upsilon_\ell^t = C_\mu \frac{k^2}{\varepsilon} + C_{\mu b} \, R_b \alpha_g |\underline{v}_r| \tag{17}$$

where [34], $C_\mu = 0.09$, and [35], $C_{\mu b} = 1.2$, and SI implies shear-induced and BI bubble-induced turbulence, respectively.

It should be noted that the asymptotic bubble-induced turbulent kinetic energy of the liquid, k_{b_a}, comes from an inviscid analysis of the relative motion between the dispersed phase and the continuous (liquid) phase. The last term in Eq. (17) is the bubble-induced viscosity enhancement model of Sato et al [35].

The virtual mass acceleration is given by [18]:

$$a_{vm} = \left(\frac{\partial}{\partial t} + \underline{v}_g \bullet \nabla\right)\underline{v}_g - \left(\frac{\partial}{\partial t} + \underline{v}_\ell \bullet \nabla\right)\underline{v}_\ell \tag{18}$$

The parameter C_D is an appropriate interfacial drag coefficient for bubbly flow, and $\overline{R}_b$ is the mean radius of the bubble. An inviscid, incompressible calculation for noninteracting spheres gives [31]: $C_{vm} = C_L = \frac{1}{2}$, $C_{vm}^* = 0$, $C_{rot} = \frac{1}{4}$, $C_1 = \frac{5}{4}$, $C_2 = -\frac{9}{20}$, $a_s = -\frac{9}{20}$, $b_s = \frac{3}{20}$.

The effect of surface tension can be modeled for small bubbles by assuming that the interface is a shell made up of nearly rigid elastic material. The role of the resultant surface type stress field is to hold the bubbles in a spherical shape. Its effect is to transfer momentum in much the same way that the stress tensor transfers stress. If we average the elastic stress equation, we have,

$$\underline{M}_{gi} = -\underline{M}_{\ell i} + \nabla \bullet \left[\alpha_g \left(\underline{\underline{\sigma}}_s + \left(p_{gi} - p_{\ell i}\right) \underline{\underline{I}}\right)\right]$$

or, partitioning into drag (d) and nondrag (nd) components:

$$\underline{M}_{gi} = -\underline{M}_{\ell i}^{(nd)} - \underline{M}_{\ell i}^{(d)} + \nabla \bullet (\alpha_g \underline{\underline{\sigma}}_s) + \nabla(\alpha_g p_{gi}) - \alpha_g \nabla p_{\ell i} \tag{19}$$

where, the surface stress tensor is [31]:

$$\underline{\underline{\sigma}}_s \stackrel{\Delta}{=} \rho_\ell \left[\hat{a}_s \underline{v}_r \underline{v}_r + \hat{b}_s (\underline{v}_r \bullet \underline{v}_r) \underline{\underline{I}}\right] \tag{20}$$

and, for a sphere:

$$\hat{a}_s = -9/20, \qquad\qquad \hat{b}_s = 3/20$$

An inviscid calculation shows [36],

$$p_{\ell i} - p_\ell = -C_p \rho_\ell |v_r|^2 \tag{21}$$

where for a rising sphere, $C_p = 0.25$. In contrast, for an oblate spheroid [37], $0.6 \leq C_p \leq 1.7$.

In addition to the closure laws derived for a free field bubbly two-phase flow, there are volumetric forces associated with turbulent dispersion $(\underline{M}_{ki}^{TD})$, wall shear $(\underline{M}_{kw})$, a wall-induced lateral force (M_{gw}^W), and, a wall-induced axial drag force on the dispersed bubbles $(\underline{M}_{gw}^D)$. The turbulent dispersion force is given in Appendix-I as,

$$\underline{M}_{\ell i}^{TD} = -\underline{M}_{gi}^{TD} = C_{TD} \, \rho_\ell \, k_\ell \, \nabla\alpha \tag{22}$$

where, k_ℓ is the total turbulent kinetic energy of the liquid phase.

A wall lift force, due to Antal et al [38], has been added to the phasic momentum equations for nodes adjacent to the walls. This force is of the form,

$$\underline{M}^W_{gw} = -\underline{M}^W_{\ell w} = \left[C_{w1} + C_{w2}\,\overline{R_b}/y\right]\frac{\alpha_g\rho_\ell}{\overline{R_b}}\,|\underline{v}_r|^2\,\underline{n}_w \tag{23}$$

Finally, volumetric wall forces having to do with the wall shear ($\underline{M}_{kw}$), are not used explicitly since the single-phase "law of the wall" is employed instead [39]. Finally, the additional axial drag on bubbles close to the wall (ie, those that are in the turbulent buffer zone) is given in Appendix-II as,

$$\underline{M}^D_{gw} = -C_{wb}\frac{\underline{v}_g\,\alpha_g}{\delta\,\overline{D_b}} \tag{24}$$

where, δ is the distance normal to the wall at which $y^+ = 5$ (ie, $\delta \cong 100\,\upsilon_\ell/<\underline{v}_\ell>$).

If needed, the mixture momentum equation can be found by adding Eqs. (8) to obtain:

$$\frac{\partial}{\partial t}(\alpha_\ell\rho_\ell\underline{v}_\ell + \alpha_g\rho_g\underline{v}_g) + \nabla\cdot\left[\alpha_\ell\rho_\ell\underline{v}_\ell\underline{v}_\ell + \alpha_g\rho_g\underline{v}_g\underline{v}_g - (a_\ell + \hat{a}_s)\alpha_g\rho_\ell\underline{v}_r\underline{v}_r\right.$$

$$\left. - \alpha_g\rho_\ell(b_\ell + \hat{b}_s)|\underline{v}_r|^2\,\underline{\underline{I}} - \alpha_\ell\underline{\underline{\tau}}^{Re}_{\ell(SI)}\right]$$

$$= -\nabla(\alpha_\ell p_\ell + \alpha_g p_g) + (\alpha_\ell\rho_\ell + \alpha_g\rho_g)\,\underline{g} - \underline{M}_{\ell w} - \underline{M}_{gw} \tag{25}$$

We note the last two terms in the spatial acceleration term account for the bubble-induced and shear-induced momentum exchanges. Interestingly, the mixture momentum equation, Eq. (25), is exactly the same as one proposed by Wallis [40].

DATA COMPARISONS

A reduced form of the three-dimensional two-fluid model has been evaluated and compared with some phase distribution upflow data for bubbly air/water flow in a pipe. For these evaluations the following values of the closure parameters were assumed [23]:

$$C_1 = C_2 = C_{vm} = C^*_{vm} = C_{rot} = a_s = \hat{a}_s = \hat{b}_s = b_s = a_\ell = b_\ell = 0.0,\ C_p = 1.0,\ C_{TD} = 0.1,\ C_{w_1} = -0.1,$$

$$C_{w_2} = 0.12,\ C_{w_b} = 1.0,\ C_L = 0.1,\ C_\mu = 0.09 \text{ and } C_{\mu_b} = 1.2.$$

The interfacial drag coefficient was given by [41],

$$C_D = 6.3/Re^{0.385}_b \tag{26}$$

where, $Re_b = \overline{D}_b\,|\underline{v}_r|/\upsilon_\ell$ and, $\overline{D}_b = 3$ mm (the measured bubble diameter).

The results of these evaluations are shown in Figs.-19 for Serizawa's air/water bubbly upflow data [2] in a pipe, and in Figs.-20 for Wang's air/water bubbly downflow data [5] in a pipe. Agreement for these values

of the closure parameters is seen to be very good. This confirms that a two-fluid model using a k-ε turbulence model and an algebraic stress law can predict lateral phase distribution in a pipe. Significantly, as can be seen in Fig.-21, **exactly the same** two-fluid model and closure relations can be used to predict the air/water bubbly upflow data of Lopez de Bertodano [23] in an isosceles triangle. Moreover, Fig.-22 shows that using virtually the same two-fluid model [38] laminar bubbly flow data can also be predicted.

These results are very exciting since they indicate that a properly formulated multidimensional two-fluid model has the inherent ability to predict lateral phase distribution phenomena in simple and complex geometry conduits for bubbles in the size range, 1 mm $\leq D_b \leq$ 6 mm.

Moreover, since the closure conditions which have been used in these predictions are physically-based, there does not seem to be any fundamental reason why the CFD approach for the analysis of multidimensional two-phase flows cannot be extended to other flow regimes and to diabatic conditions. Indeed, such extensions will only require the development of new closure conditions which are appropriate for the particular multiphase situations being studied.

SUMMARY AND CONCLUSIONS

It has been shown that pronounced lateral phase distribution may occur in simple complex geometry conduits. Significantly, a multidimensional two-fluid model, and its associated closure conditions, were numerically evaluated using the PHOENICS code, and gave results that agreed with the bubbly flow phase distribution data taken in both simple and complex geometry conduits. Moreover, it appears that this approach may be extended to flow regimes other than just bubbly flows, and should also be able to accommodate phase change effects.

It seems that we may be on the threshold of a major revolution in the way multiphase flows are analyzed. Indeed, it appears that the CFD evaluations of multidimensional two-fluid models have the inherent capability to replace many of the empirically-based analyses in use today. It is hoped that this paper will help stimulate multiphase researchers to actively participate in this scientific revolution so that reliable mechanistic multiphase flow CFD evaluations for all flow regimes of interest will be possible in the foreseeable future.

ACKNOWLEDGMENT

REFERENCES

[1]   R.T Lahey, Jr., The analysis of phase separation and phase distribution phenomena using two-fluid models, Nuc. Engrg. & Des. 122 (1990) 17-40.

[2]   A. Serizawa, I. Kataoka and I. Michiyoshi, Turbulent structure of air/water bubbly flow, Int. J. Multiphase Flow 2(3) (1975) 221-234.

[3]   I. Michiyoshi and A. Serizawa, Turbulence in two-phase bubbly flow, Nuc. Eng. & Des. 95 (1986) 253-267.

[4]   N.V. Valukina, B.K. Koz'menko and O.N. Kashinskii, Characteristics of a flow of monodisperse gas-liquid mixture in a vertical tube, Inzhenerno-Richenskii Zhurnal 36(4) (1979) 695-699.

[5]   S.K. Wang, S.J. Lee, O.C. Jones, Jr. and R.T. Lahey, Jr., 3-D turbulence structure and phase distribution measurements in bubbly two-phase flows Int. J. Multiphase Flow 13(3) (1987) 327-343.

[6]   G. Class, R. Meyder and W. Sengpiel, Measurement of spatial gas distribution and turbulence structure in developing bubbly two-phase in vertical channels, Proceedings of the International Conference on Multiphase Flows '91 - Tsukuba 1 (1991) 473-477.

[7]   T.J. Liu, The effect of bubble size on void fraction distribution ina vertical channel, Proceedings of the International Conference on Multiphase Flows '91 - Tsukuba 1 (1991) 453-457.

[8]   K. Sekoguchi, T. Sato and T. Honda, Two-phase bubble flow (first report), Trans. Japan Soc. Mech. Engng. 40(333) (1974) 1395-1403.

[9]   I. Žun, Transition from wall void peaking to core void peaking in turbulent bubbly flow, Proceedings of the ICHMT Seminar on Transient Phenomena in Multiphase Flow (Dubrovnik, Yugoslavia, 1987).

[10]   H. Monji and G. Matsui, Effect of bubble size on the structure of vertical bubble flow, Proceedings of the International Conference on Multiphase Flows '91 - Tsukuba 1 (1991) 449-452.

[11]   M. Sadatomi, T. Sato and S. Saruwatari, Two-phase flow in vertical noncircular channels, Int. J. Multiphase Flow 8(6) (1982) 641-655.

[12]   S.K. Sim and R.T. Lahey, Jr., Measurement of phase distribution in a triangular conduit, Int. J. Multiphase Flow 12(3) (1986) 405-425.

[13]   K. Ohkawa and R.T. Lahey, Jr., An experimental investigation of phase distribution in an eccentric annulus, Int. J. Multiphase Flow 15(3) (1989) 447-457.

[14]   B. Shiralkar and R.T. Lahey, Jr., Diabatic local void fraction measurements in Freon-114 with a hot wire anemometer, ANS Trans. 15(2) (1972) 880.

[15]   D. Drew and R.T. Lahey, Jr., Phase distribution mechanisms in turbulent two-phase flow in a circular pipe, J. Fluid Mech. 117 (1982) 91-106.

[16]   D. Drew and R.T. Lahey, Jr., Phase distribution mechanisms in turbulent two-phase flow in channels of arbitrary cross section, J. Fluid Engng. 203 (1981) 583-589.

[17]   I. Kataoka and A. Serizawa, Statistical behavior of bubbles and its application to prediction of phase distribution in bubbly two-phase flow, Proceedings of the International Conference on Multiphase Flows '91 - Tsukuba 1 (1991) 459-462.

[18]   D.A. Drew and R.T. Lahey, Jr., The virtual mass and lift force on a sphere in rotating and straining flow, Int. J. Multiphase Flow 13(7) (1987) 113-121.

[19]   D.A. Drew and R.T. Lahey, Jr., Some supplemental analysis concerning the virtual mass and lift force on a sphere in a rotating and straining flow, Int. J. Multiphase Flow 16(6) (1990) 1127-1130.

[20]   I. Žun and Može S. Kljenak, Space-time evaluation of bubble nonhomogeneous distribution in upward flow, Proceedings of the International Conference on Multiphase Flows '91 - Tsukuba 1 (1991) 463-466.

[21]   S-J. Lee, R.T. Lahey, Jr. and O.C. Jones, Jr., The prediction of two-phase turubulence and phase distribution phenomena using a K-ε model, Japanese Journal of Multiphase Flow 3(4) (1989) 335-368.

[22]   M. Lopez de Bertodano, S-J. Lee, R.T. Lahey, Jr. and D.A. Drew, The prediction of two-phase turbulence and phase distribution using a Reynolds stress model, J. Fluids Eng. 112 (1990) 107-113.

[23]   M. Lopez de Bertodano, Turbulent bubbly two-phase flow in a triangular duct, PhD Thesis, Rensselaer Polytechnic Institute, Troy, NY (1992).

[24]   A.N. Kolmogorov, The local structure of turbulence in incompressible viscous fluid for very large Reynolds number, Comptes Rendres (Doklady) de l'Academie des Sciences de l'URSS 31, (1941) 538-540.

[25]   S-K. Sim and R.T. Lahey, Jr., The measurement of phase distribution phenomena in a triangular duct, NUREG/CR-3576 (1983).

[26]   S-J. Lee, S.K. Wang, O.C. Jones & R.T. Lahey, Jr., Local void fraction measurement techniques in two-phase bubbly flows using hot-film anemometry, Proc. 22nd ASME Annual Heat Transfer Conference, Niagara Falls, NY (1984).

[27]   S.K. Wang, Three-dimensional turbulence structure measurements in air-water two-phase flow, Ph.D. Thesis, Rensselaer Polytechnic Institute, Troy, New York (1985).

[28]   F.E. Jorgensen, Directional sensitivity of wire and fiber-film probes, DISA Information, No. 11 (1971) 31-37.

[29]   R.T. Lahey, Jr. and D.A. Drew, The current state-of-the-art in the modeling of vapor/liquid two-phase flow, ASME Reprint, 90-WA/HT-13 (1990).

[30]   G. Arnold, D.A. Drew and R.T. Lahey, Jr., Derivation of constitutive equations for interfacial force and Reynolds stress for a suspension of spheres using ensemble averaging, Chem. Eng. Comm. 86 (1989) 43-54.

[31]   J-W. Park, Void wave propagation in two-phase flow, PhD Thesis, Rensselaer Polytechnic Institute, Troy, NY (1992).

[32]   R.I. Nigmatulin, Spatial averaging in the mechanics of heterogeneous and dispersed systems, Int. J. Multiphase Flow 5 (1979) 353.

[33]   A. Biesheuvel and L. van Wijngaarden, Two-phase flow equations for a dilute dispersion of gas bubbles in liquid, J. Fluid Mech. 168 (1984) 301-318.

[34]   W. Rodi, Turbulence Models and Their Applications in Hydraulics, IAHR/AIRH Monograph (1984).

[35]   Y. Sato, M. Sadatomi and K. Sekoguchi, Momentum and heat transfer in two-phase bubbly flow-I, Int. J. Multiphase Flow 7(2) (1981) 167-178.

[36]   H. Lamb, Hydrodynamics, Dover Publications, New York (1932).

[37]   M. Lance and J. Bataille, Turbulence in the liquid phase of a uniform bubbly air-water flow, J. Fluid Mech. 22 (1991) 95-118.

[38]   S.P. Antal, R.T. Lahey, R.T. and J.E. Flaherty, J.E., Analysis of phase distribution in fully developed laminar bubbly two-phase flow, Int. J. Multiphase Flow 17(5) (1991) 635-652.

[39]   J.L. Marié, Modeling of the skin friction and heat transfer in turbulent two-component bubbly flow in pipes, Int. J. Multiphase Flow 13(3) (1987) 309-326.

[40]   G.B. Wallis, Inertial coupling in two-phase flow: macroscopic properties of suspensions in an inviscid fluid, Multiphase Science & Technology, Vol. V, eds. G.F. Hewitt, J-M. Delhaye & N, Zuber (Hemisphere, New York, 1990) pp. 239-361.

[41]   G.B. Wallis, Inertial coupling in two-phase flow: macroscopic properties of suspensions in an inviscid fluid, Multiphase Science & Technology Vol. 5, eds. G. Hewitt, J-M. Delhaye & N. Zuber (Hemisphere, New York, 1991), pp. 239-361.

APPENDIX-I: TURBULENT DISPERSION FORCE

The motivation to develop a turbulent dispersion force comes from the fact that the averaged two-phase continuity equations do not allow for a phasic diffusion term. That is, since the volume fraction of phase-k, α_k, is defined as an average, terms such as α_k' do not exist. In contrast, a dispersion force in the momentum equations may occur.

The averaged continuity equation of phase-k, assuming no phase source, is:

$$\frac{\partial}{\partial t}\overline{X_k} + \nabla\cdot\overline{X_k \underline{v}_k} = 0 \tag{I.1}$$

where X_k is the phase indicator function and $\underline{v}_k$ is the instantaneous phasic velocity. Notice that this is a natural way to average because both these quantities are what a hot film anemometer actually measures. Then by defining:

$$\alpha_k = \overline{X_k} \tag{I.2}$$

and,

$$\underline{v}_k = \frac{\overline{X_k \underline{v}_k}}{\overline{X_k}} \tag{I.3}$$

the continuity equation becomes:

$$\frac{\partial}{\partial t}\alpha_k + \nabla\cdot\alpha_k\,\underline{v}_k = 0 \tag{I.4}$$

Other investigators have started from this equation and averaged once more to obtain:

$$\frac{\partial}{\partial t}\overline{\alpha_k} + \nabla\cdot\overline{\alpha}_k\,\underline{v}_k + \nabla\cdot\overline{\alpha_k'\underline{v}_k'} = 0 \tag{I.5}$$

where the last term on the left hand side of Eq. (I.5) allowed them to have a turbulent diffusion term in the continuity equation. Unfortunately, as discussed above, this is not rigorous. However, we may have a turbulent diffusion force in the momentum equations.

In order to derive a turbulent dispersion force an analogy is made with the thermal diffusion of air molecules in the atmosphere. If it were not for the thermal kinetic energy of the air molecules the atmosphere would be very thin indeed since all the air molecules would be held against the ground by gravity. The thermal motion that keeps the molecules away from the ground may be thought of as a thermal diffusion force that acts against gravity. A Gedanken (ie, thought) experiment can then be made for a bounded turbulent bubbly mixture whose dispersion is similar to that of air molecules, except that the motion of the bubbles is produced by the turbulent energy of the liquid phase instead of the thermal energy of the air molecules.

Let us begin by analyzing the earth's atmosphere. The momentum equation applied to a stagnant atmosphere is:

$$\frac{d\,p}{dy} = -\rho g \tag{I.6}$$

For isothermal conditions:

$$\frac{p}{p_0} = \frac{\rho}{\rho_0} \tag{I.7}$$

so the solution to the momentum equation becomes:

$$\frac{\rho}{\rho_0} = \exp\left(-\frac{\rho_0}{p_0} g\, y\right) \tag{I.8}$$

Applying the perfect gas law:

$$\frac{\rho}{\rho_0} = \exp\left(-\frac{gy}{RT}\right) \tag{I.9}$$

Since the number density of air molecules (n''') is proportional to the mass density:

$$\frac{n'''}{n_0'''} = \exp\left(-\frac{gy}{RT}\right) = \exp\left(-\frac{\phi}{RT}\right) \tag{I.10}$$

where ϕ is the gravitational potential (gy) and RT is the thermal kinetic energy of the air molecules. Thus,

$$\phi = -RT \ln \frac{n'''}{n_0'''} \tag{I.11}$$

and the gravitational force is:

$$F_g = -\nabla\phi = RT\, \nabla \ln n''' = -g \tag{I.12}$$

Then the dispersion force, F_D, is such that,

$$F_g + F_D = 0 \tag{I.13}$$

Hence,

$$F_D = -RT\, \nabla \ln n''' \tag{I.14}$$

By analogy the turbulent dispersion force per unit mass on the bubbles becomes,

$$F_{TD} = -C_{TD}\, k\, \nabla \ln \alpha \tag{I.15}$$

where C_{TD} is a proportionality factor.

An equivalent force on the liquid phase is:

$$F_{TD} = -C_{TD}\, k_\ell \nabla \ln (1 - \alpha) \tag{I.16}$$

Thus the volumetric turbulent void dispersion force is:

$$M_{\ell i}^{TD} = -M_{vi}^{TD} = -C_{TD}\, \rho_\ell\, (1-\alpha)\, k_\ell \nabla \ln (1-\alpha) = C_{TD}\, \rho_\ell\, k_\ell \nabla \alpha \tag{I.17}$$

APPENDIX-II: AXIAL WALL FORCE ON BUBBLES

As observed by Marié et.al. [39], because of the finite size of the bubbles and the steep velocity gradient near the wall, there is an axial wall force on the bubbles near the wall. It is proposed that there is a region of close contact between the bubble and the wall and beneath the bubble the liquid film thickness is of the order of the laminar sublayer thickness. Hence the wall shear force on the bubble is:

$$F_{gw}^D = - A \mu_\ell \frac{dv_\ell}{dy} \cong - A \mu_\ell \frac{dv_g}{dy} \tag{II.1}$$

where A is the shear area beneath the bubble, y is the laminar sublayer thickness and v_g is the local mean bubble velocity. This may be converted to a force per unit volume:

$$M_{gw}^D = F_{gw}^D \frac{\alpha}{\frac{\pi}{6} \overline{D}_b^3} \cong - \mu_\ell \frac{v_g}{y} \alpha \frac{A}{\frac{\pi}{6} \overline{D}_b^3} \tag{II.2}$$

Finally, letting the shear area, A, be a function of the bubble cross sectional area, $\frac{\pi}{4} D_b^2$, yields:

$$M_{gw}^D = - C_{wb} \mu_\ell \frac{v_g}{\delta} \frac{\alpha}{D_b} \tag{II.3}$$

The laminar sublayer thickness is defined as:

$$\delta^+ = \frac{\delta v_*}{v_\ell} = 5 \tag{II.4}$$

and since[†]

$$v^* \cong 0.05 \left| <v_\ell> \right| \tag{II.5}$$

then the thickness of the laminar sublayer is:

$$\delta \cong 100 \frac{v_\ell}{\left| <v_\ell> \right|} \tag{II.6}$$

Inserting Eq. (II.6) into Eq. (II.3) yields:

$$M_{gw}^D = - C_{wb} \frac{\rho_\ell}{100 D_b} \alpha \left| <v_\ell> \right| v_g \tag{II.7}$$

[†] $v_* = \sqrt{\tau_w/\rho_\ell} = \sqrt{c_f/2} <v_\ell>$

where, $c_f \cong 0.005$
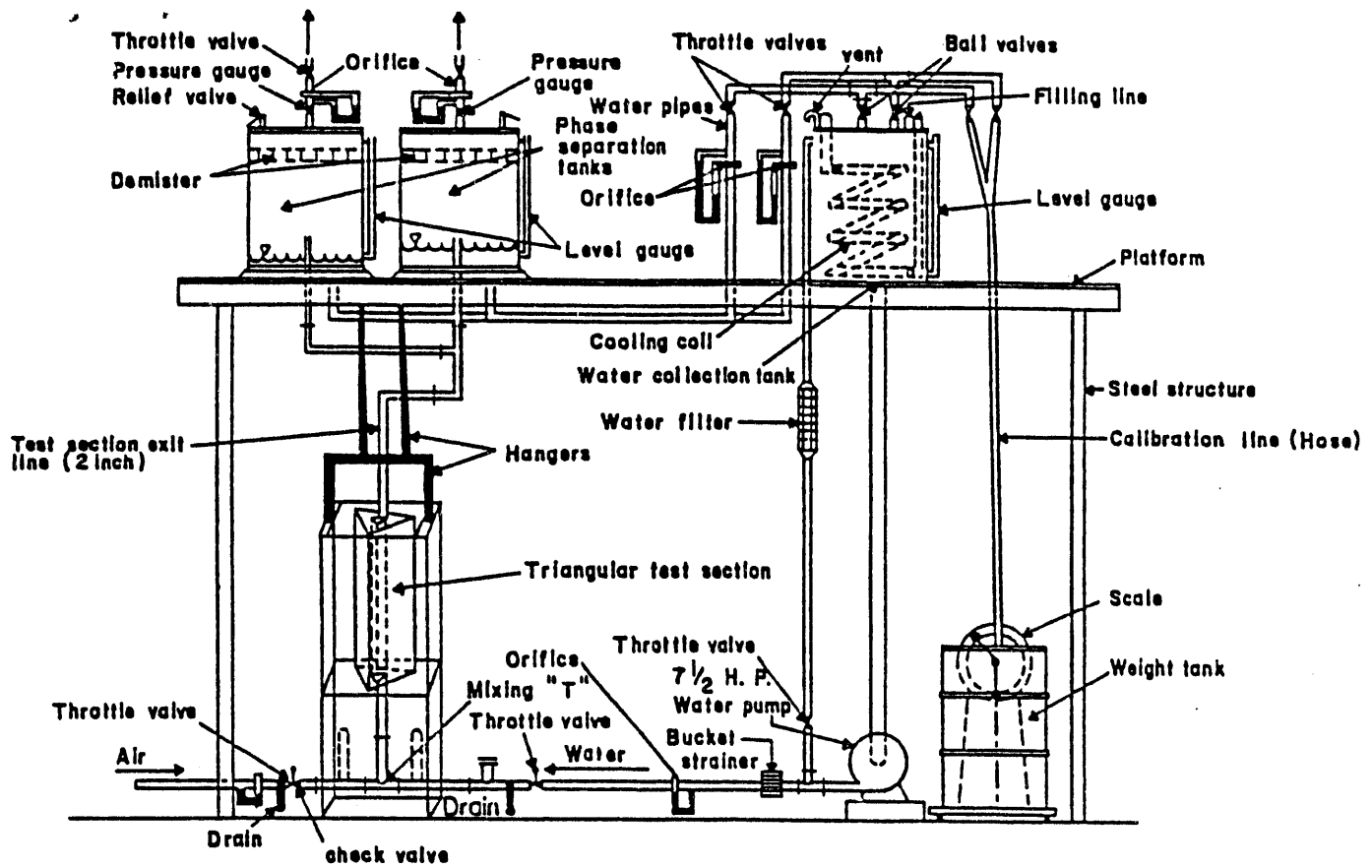
Fig. 1 Schematic of Air/Water Loop
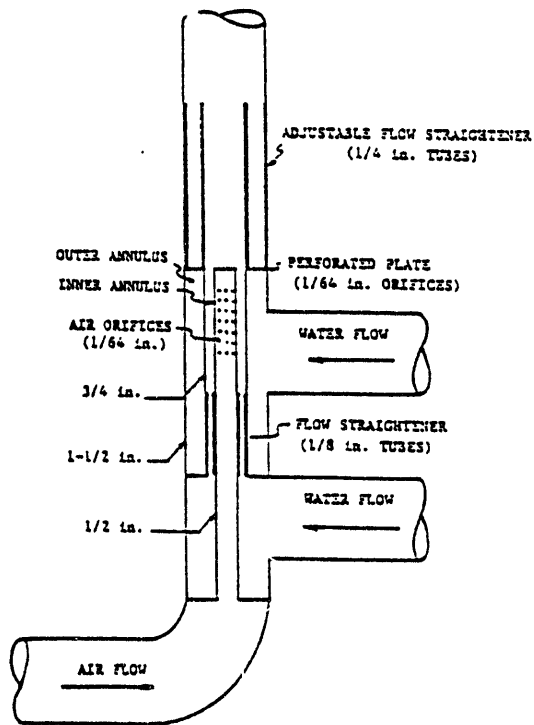
Fig. 2 Schematic of Mixing Tee
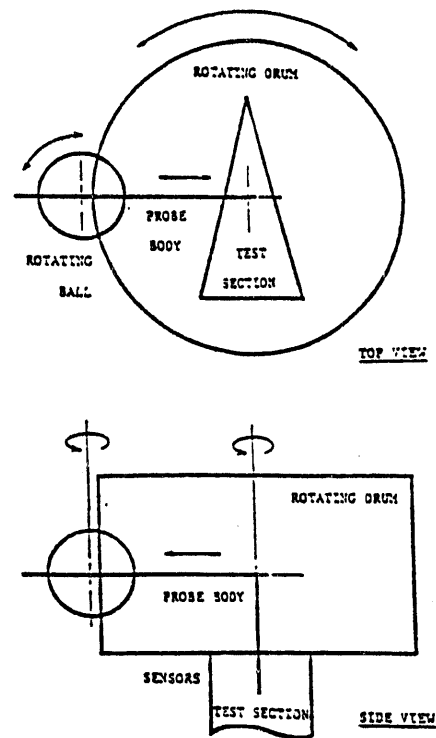
Fig. 3 Schematic of Traversing Mechanism
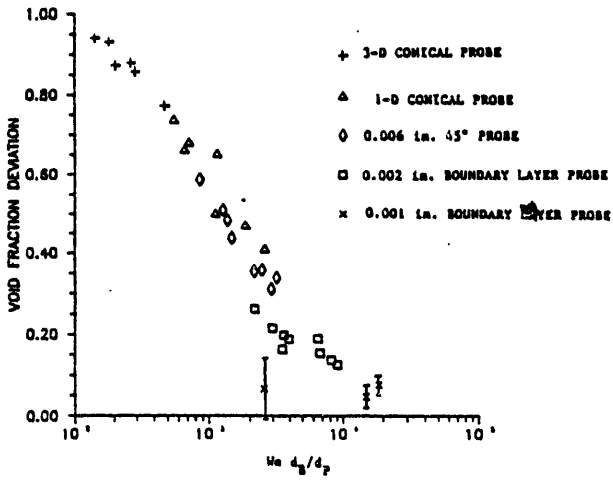
Fig. 4 Void Fraction Measurement Error with Hot Film Probes
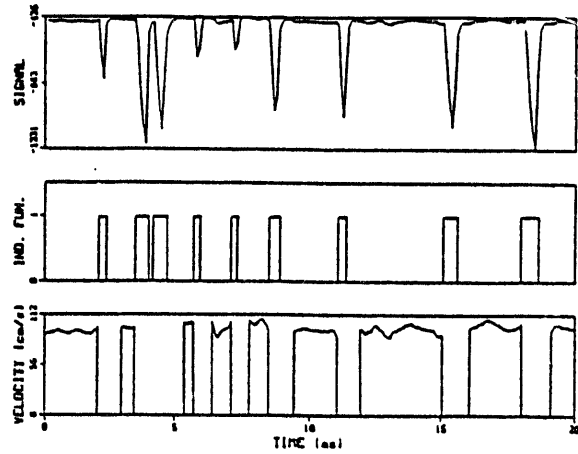
Fig. 5 Probe Signal and Processed Data
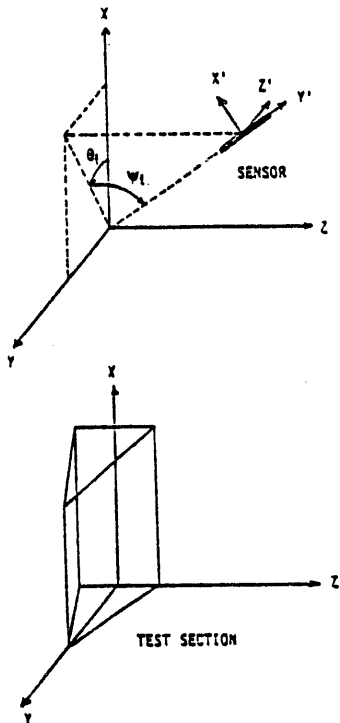
Fig. 6 Sensor Coordina_ ystem
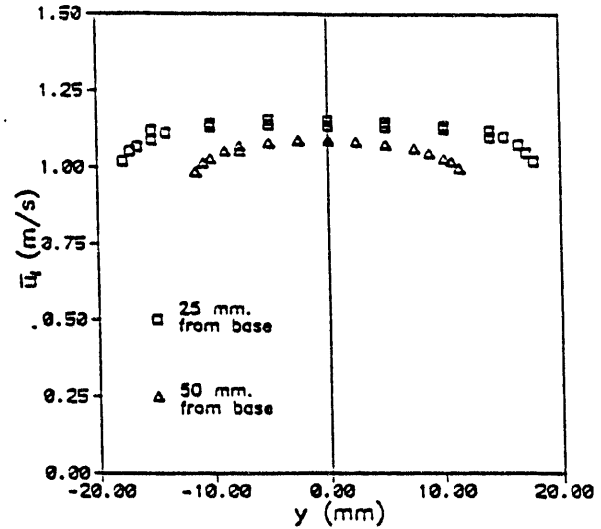
Fig. 7 Velocity Symmetry Test (j_ℓ = 1.0 m/s; j_g = 0.1 m/s)
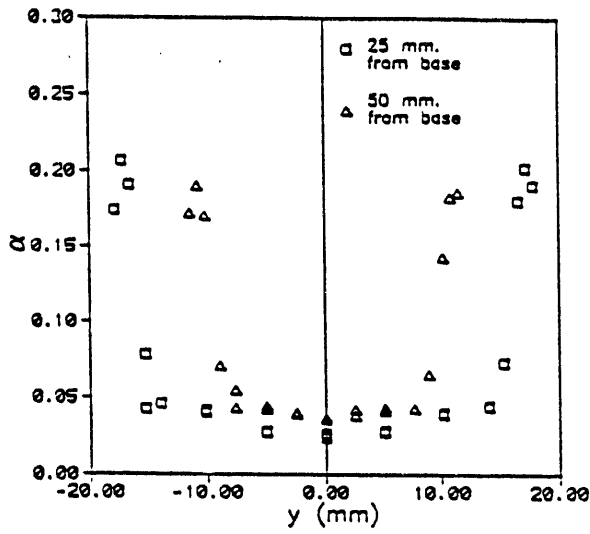
Fig. 8 Void Fraction Symmetry Test (j_ℓ = 1.0 m/s; j_g = 0.1 m/s)
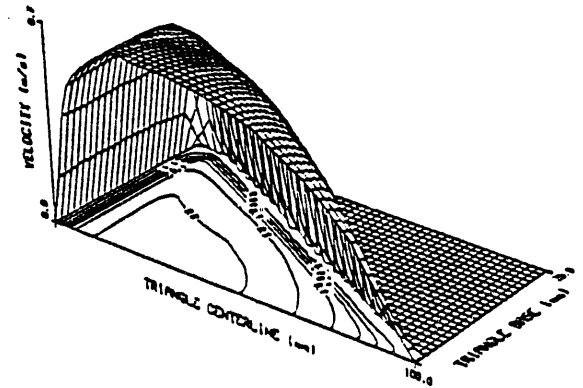
Fig. 9 Liquid Velocity Distribution (j_ℓ = 0.5 m/s; j_g = 0.0 m/s)
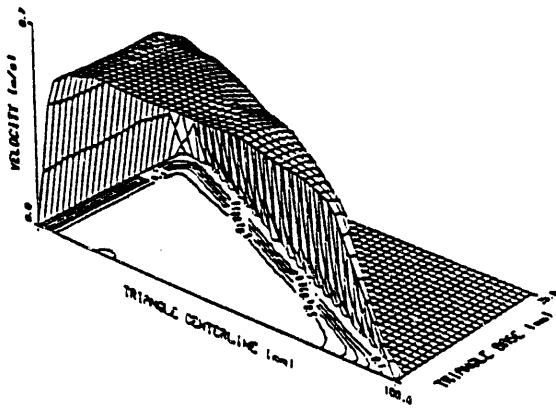
Fig. 10 Liquid Velocity Distribution (j_ℓ = 0.5 m/s; j_g = 0.05 m/s)
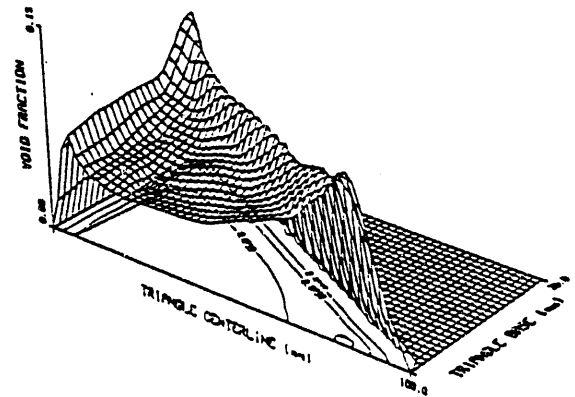
Fig. 11 Void Fraction Distribution (j_ℓ = 0.5 m/s; j_g = 0.05 m/s)
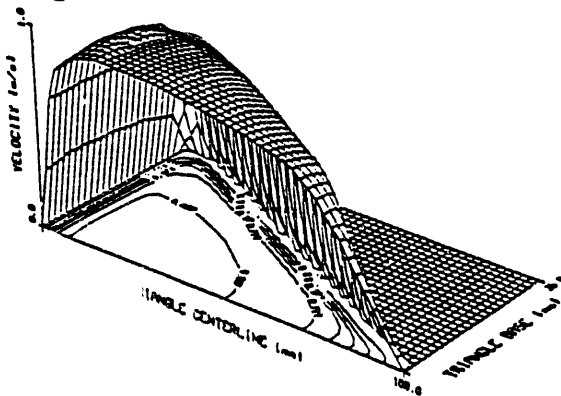
Fig. 12 Liquid Velocity Distribution (j_ℓ = 0.5 m/s; j_g = 0.4 m/s)
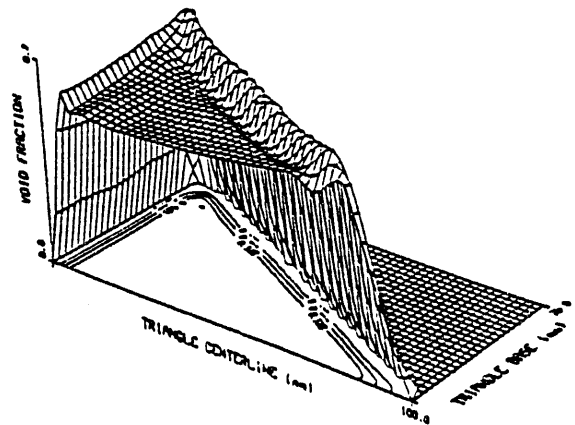
Fig. 13 Void Fraction Distribution (j_ℓ = 0.5 m/s; j_g = 0.4 m/s)
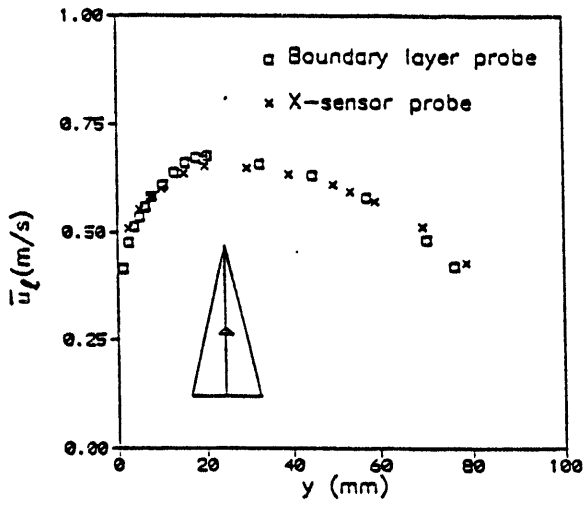
Fig. 14 Comparison Between Boundary Layer Probe and X-Sensor Probe (j_ℓ = 0.5 m/s; jg = 0.0 m/s)
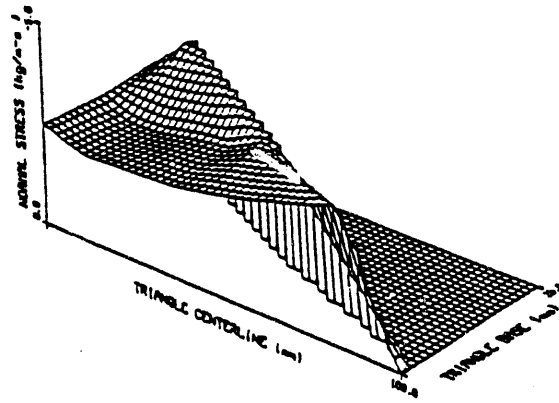
Fig. 15 $-\rho_\ell\overline{v'v'}$ Distribution (j_ℓ = 0.5 m/s; jg = 0.05 m/s)
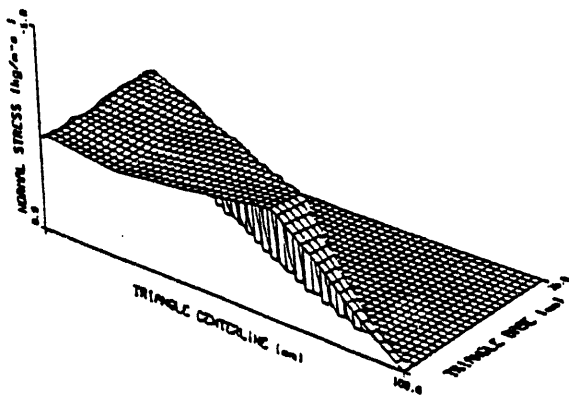
Fig. 16 $-\rho_\ell\overline{w'w'}$ Distribution (j_ℓ = 0.5 m/s; jg = 0.05 m/s)
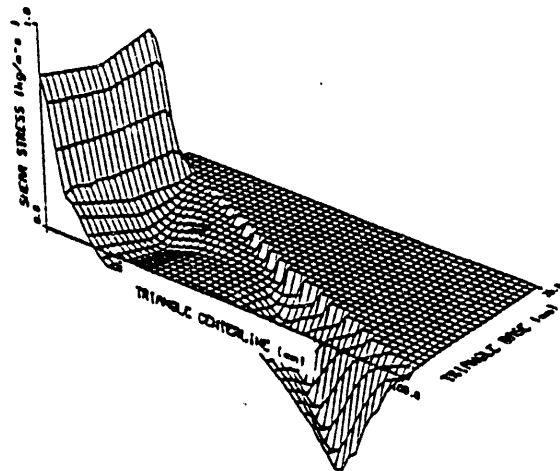
Fig. 17 $-\rho_\ell\overline{u'v'}$ Distribution (j_ℓ = 0.5 m/s; jg = 0.05 m/s)
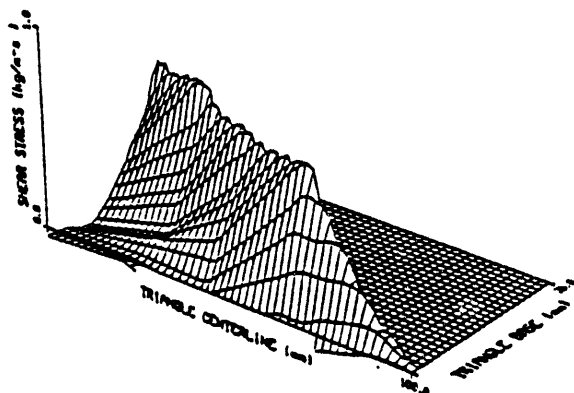
Fig. 18 $-\rho_\ell\overline{u'w'}$ Distribution (j_ℓ = 0.5 m/s; jg = 0.05 m/s)
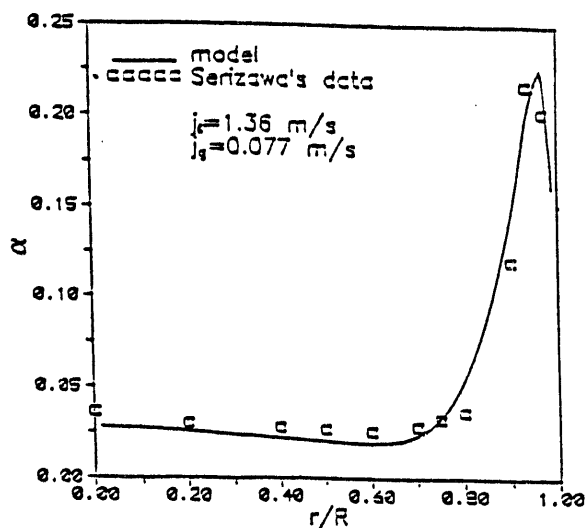
Fig. 19a Void Fraction Comparison with Seriwaza's Upflow Data [2]: (j_ℓ = 1.36 m/s; j_g = 0.077 m/s; D_b = 3 mm; C_L = 0.1; C_p = 1.0)
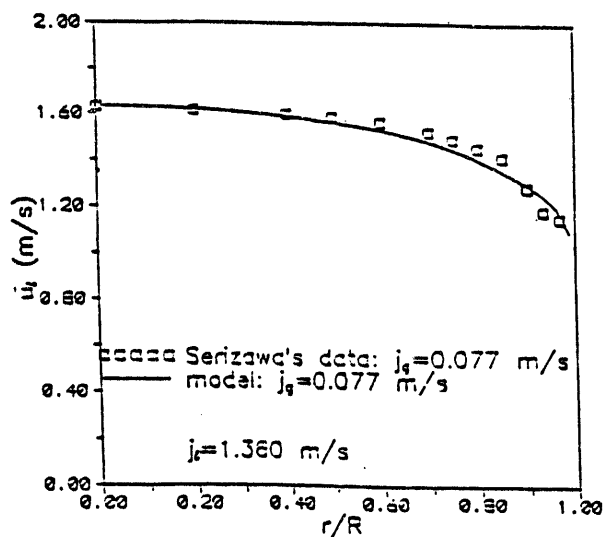
Fig. 19b Mean Axial Liquid Velocity Comparison with Seriwaza's Upflow Data [2]: (j_ℓ = 1.36 m/s; j_g = 0.077 m/s; D_b = 3 mm; C_L = 0.1; C_p = 1.0)
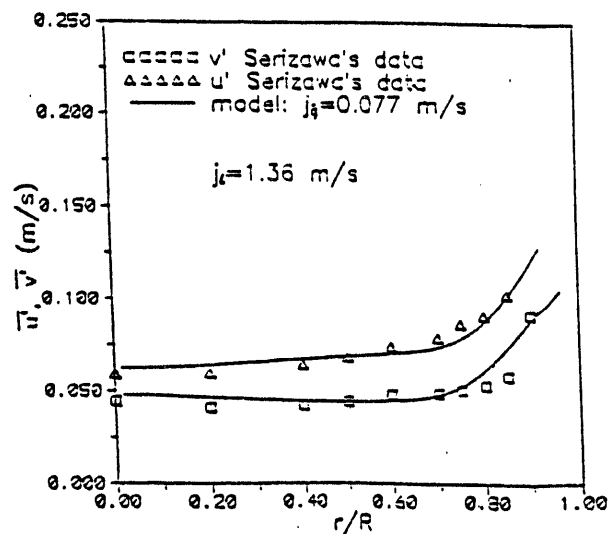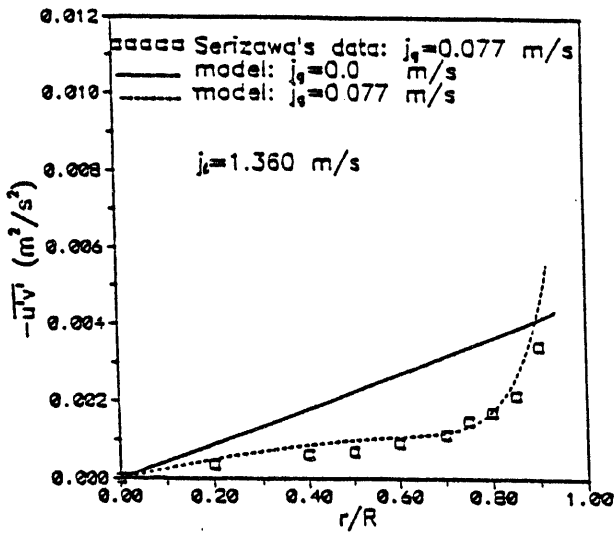

Fig. 19c Liquid Phase Turbulent Velocity Fluctuation Comparison with Seriwaza's Upflow Data [6]: (j_ℓ = 1.36 m/s; j_g = 0.077 m/s; D_b = 3 mm; C_L = 0.1; C_p = 1.0)

19

Fig. 19d   Liquid Phase Reynolds Stress Comparison with Seriwaza's Upflow Data [2]: (j_ℓ = 1.36 m/s; j_g = 0.077 m/s; D_b = 3 mm; C_L = 0.1; C_p = 1.0)

Fig. 21 Void: Comparison with Lopez's Upflow Data in a Triangle [23]: (j_ℓ = 1.0 m/s; j_g = 0.1 m/s; C_L = 0.1; C_p = 1.0)
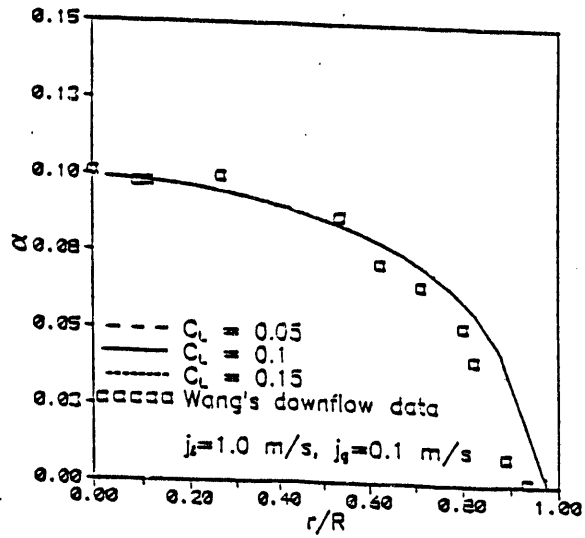

Fig. 20 Void Fraction Comparison with Wang's Downflow Data [5]: The Effect of Lift (C_p = 1.0; C_L = 0.1; D_b = 3 mm)
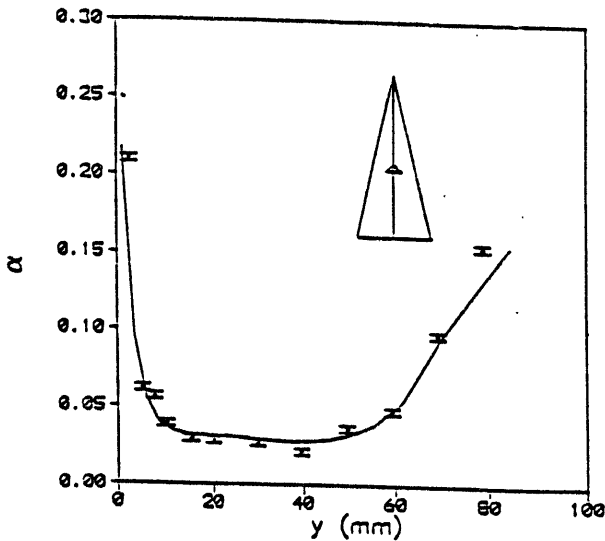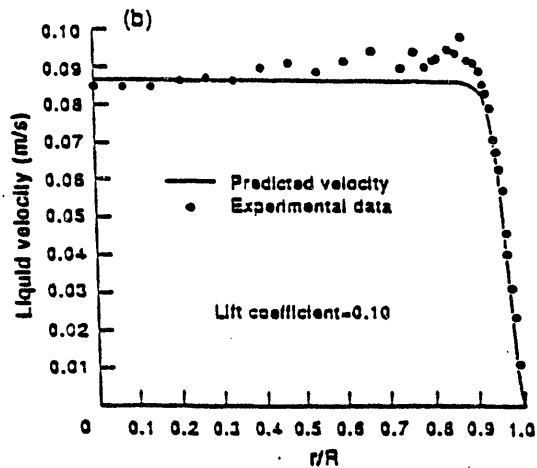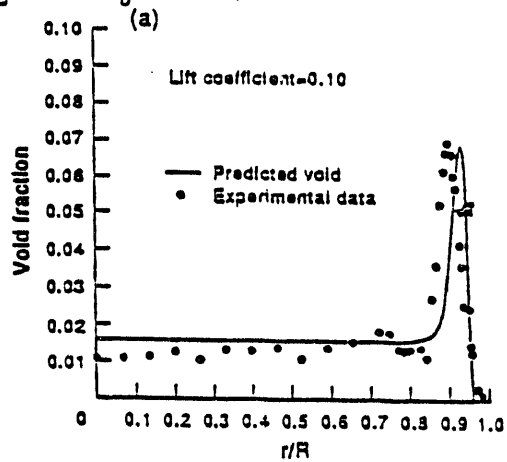

Fig. 22 Comparison with Laminar Bubbly Flow Data [38]: (Re_ℓ = 1276, p_ℓ = 1 Atms)

END

DATE FILMED

3/21/94